CrossMark

ORIGINAL PAPER

Surface Spectroscopy on UHV-Grown and Technological Ni–ZrO₂ Reforming Catalysts: From UHV to Operando Conditions

Kresimir Anic[1] · Astrid Wolfbeisser[1] · Hao Li[1] · Christoph Rameshan[1] · Karin Föttinger[1] · Johannes Bernardi[2] · Günther Rupprechter[1]

Abstract Ni nanoparticles supported on ZrO_2 are a prototypical system for reforming catalysis converting methane to synthesis gas. Herein, we examine this catalyst on a fundamental level using a 2-fold approach employing industrial-grade catalysts as well as surface science based model catalysts. In both cases we examine the atomic (HRTEM/XRD/LEED) and electronic (XPS) structure, as well as the adsorption properties (FTIR/PM-IRAS), with emphasis on in situ/operando studies under atmospheric pressure conditions. For technological Ni–ZrO_2 the rather large Ni nanoparticles (about 20 nm diameter) were evenly distributed over the monoclinic zirconia support. In situ FTIR spectroscopy and ex situ XRD revealed that even upon H_2 exposure at 673 K no full reduction of the nickel surface was achieved. CO adsorbed reversibly on metallic and oxidic Ni sites but no CO dissociation was observed at room temperature, most likely because the Ni particle edges/steps comprised Ni oxide. CO desorption temperatures were in line with single crystal data, due to the large size of the nanoparticles. During methane dry reforming at 873 K carbon species were deposited on the Ni surface within the first 3 h but the CH_4 and CO_2 conversion hardly changed even during 24 h. Post reaction TEM and TPO suggest the formation of graphitic and whisker-type carbon that do not significantly block the Ni surface but rather physically block the tube reactor. Reverse water gas shift decreased the H_2/CO ratio. Operando studies of methane steam reforming, simultaneously recording FTIR and MS data, detected activated CH_4 (CH_3 and CH_2), activated water (OH), as well as different bidentate (bi)carbonate species, with the latter being involved in the water gas shift side reaction. Surface science Ni–ZrO_2 model catalysts were prepared by first growing an ultrathin "trilayer" (O–Zr–O) ZrO_2 support on an Pd_3Zr alloy substrate, and subsequently depositing Ni, with the process being monitored by XPS and LEED. Apart from the trilayer oxide, there is a small fraction of ZrO_2 clusters with more bulk-like properties. When CO was adsorbed on the (fully metallic) Ni particles at pressures up to 100 mbar, both PM-IRAS and XPS indicated CO dissociation around room temperature and blocking of the Ni surface by carbon (note that on the partially oxidized technological Ni particles, CO dissociation was absent). The Ni nanoparticles were stable up to 550 K but annealing to higher temperatures induced Ni migration through the ultrathin ZrO_2 support into the Pd_3Zr alloy. Both approaches have their benefits and limitations but enable us to address specific questions on a molecular level.

Keywords Nickel · Zirconia · Model catalysts · Technological catalysts · Carbon monoxide · Methane steam reforming · Methane dry reforming · In situ spectroscopy · Operando spectroscopy

✉ Günther Rupprechter
guenther.rupprechter@tuwien.ac.at

1 Institute of Materials Chemistry, Technische Universität Wien, Getreidemarkt 9/BC/01, 1060 Vienna, Austria

2 University Service Center for Transmission Electron Microscopy, Technische Universität Wien, Wiedner Hauptstraße 8-10, 1040 Vienna, Austria

1 Introduction

Ni–ZrO_2 catalysts are among the most important industrial catalysts, due to their widespread application for methane reforming reactions. Steam reforming [1–3], dry reforming [4–9] and partial oxidation [10, 11] are routes to produce

synthesis gas (CO and H$_2$) of varying composition but in all cases deactivation by coke (carbon filament) formation is a major limitation of catalyst performance and lifetime. Several strategies were applied to reduce coking, including alloying with a second metal (e.g. Au [12–14], Cu [15–25], intended to decorate the active Ni steps that are prone to coking with a less active metal) and/or using mixed-oxide supports [4, 5, 26–33]. Adding CeO$_2$ to ZrO$_2$ to has been found to improve the oxygen storage capacity and redox properties, which affects the ability to deliver oxygen from the lattice to carbon, increasing thermal stability and catalytic activity [3, 5, 26].

Apart from these modified variants, the "simple" Ni–ZrO$_2$ catalysts still holds potential for fundamental studies of the nanoparticle size, shape and surface structure, of the interaction of the Ni nanoparticles with the oxide support, of the specific adsorption and reaction properties of metal-, oxide- and metal-oxide-interface sites, and of the thermal and chemical stability of the catalysts. Due to the relatively harsh reforming conditions, especially high temperature, the exact reaction mechanisms on Ni (and Pt) are still debated [34–39]. Herein, we describe an approach to examine fundamental properties of Ni–ZrO$_2$ by performing surface spectroscopic studies both on technological and model (ultrahigh vacuum (UHV) prepared) catalysts. Whereas the first provide a link to industrial catalysis, the latter enable us to reduce complexity and to apply surface science techniques [40–51].

It is important to note that in both cases structure, composition and adsorption properties were examined which clearly reveals analogies but also differences between applied and model catalysts. For both types of catalysts we have performed "in situ" studies, i.e. acquiring surface spectra during ongoing processes, in an effort to obtain meaningful and technologically relevant structure–activity correlations. In recent years we have applied this approach to a variety of technological catalysts [52–58] and single-crystal based model catalysts [59–61]. For the technological catalysts, when catalytic activity is recorded simultaneously, the term "*operando*" spectroscopy is rather used [62, 63].

2 Experimental

In the following, the synthesis/preparation of the Ni–ZrO$_2$ catalysts is briefly described. For more detailed descriptions we refer to refs [24, 25].

2.1 Impregnated Ni–ZrO$_2$

The technological Ni–ZrO$_2$ catalyst was prepared by impregnation of ZrO$_2$ (commercial Zr(OH)$_4$ from MEL chemicals XZO 880/01; calcined at 973 K) with a total metal weight content of 5 % w/w. After dissolving the appropriate amount of Ni-nitrate in water, ZrO$_2$ powder was suspended in the solution, which was dried at 373 K overnight. Then the powder was heated to 723 K in air with a heating rate of 5 K min^{-1} and calcined at 723 K for 2 h. Prior to characterization and reaction the catalyst was oxidized at 773 K and reduced at 673 K (at ∼1 bar in 20 % O$_2$ in Ar and 20 % H$_2$ in Ar, respectively, with a flow rate 50 ml min^{-1}).

The catalyst was characterized by high resolution transmission electron microscopy (HRTEM) including energy dispersive X-ray fluorescence (EDX) analysis, H$_2$-chemisorption, infrared spectroscopy (FTIR) with CO as a probe molecule, X-ray diffraction (XRD), and X-ray absorption spectroscopy (XAS). To study the catalytic performance, the catalyst was tested in a continuous flow setup for methane dry and steam reforming. Operando spectroscopy provides information about the catalyst under reaction conditions, i.e. high temperature and reactive gas atmosphere. In this respect, operando IR, XAS and near atmospheric pressure X-ray photoelectron (NAP-XPS) spectroscopy were applied. After reaction, the used catalyst was further studied via temperature programmed oxidation (TPO), in order to get information about the amount of carbon deposition and the temperature needed to remove the carbon species via oxidation, and by HRTEM, imaging carbon deposition.

2.2 Ni Nanoparticles on Ultrathin ZrO$_2$ Films Grown in UHV

The experimental setup used to prepare and characterize the ultrathin ZrO$_2$ support, as well as the Ni nanoparticles, has been described in detail in references [49, 50]. In brief, it consists of an ultrahigh vacuum (UHV) chamber for sample preparation and characterization (LEED, TPD, XPS, IRAS), which is connected to a UHV-compatible atmospheric pressure reaction cell ("Rupprechter-design" [64]) that also allows for in situ PM-IRAS spectroscopy. In order to prepare an ultrathin model zirconia thin film with Ni nanoparticles on top, either a Pd$_3$Zr(0001) or Pt$_3$Zr(0001) single crystal was cleaned by sputtering (8 × 10^{-6} mbar of Ar, 2 kV) and annealing in UHV. After cleaning, the Pd$_3$Zr or Pt$_3$Zr single crystal was exposed to 1 × 10^{-7} mbar of O$_2$ at 673 K for 30 min, followed by annealing in UHV at 1073 K for 20 min to grow an uniform ultrathin ZrO$_2$ layer (for details see [65, 66]). On top of this ultrathin layer, an amount of Ni equivalent to a homogeneous layer of nominally 3 Å was deposited at room temperature, utilizing an Omicron electron-beam triple evaporator (EFM 3T) for physical vapor deposition. The prepared model catalyst surface was characterized by

LEED and XPS and, to follow the interaction of the surface with CO, by polarization modulation infrared reflection absorption spectroscopy (PM-IRAS) [67].

3 Results and Discussion

The following section is divided into two parts, the first describing results obtained for the technological catalyst, and the second describing those for the model catalyst. For both we first focus on structural properties, then turn to CO adsorption properties, and finally discuss studies performed under elevated pressure and/or elevated temperature conditions.

3.1 Technological Ni–ZrO$_2$

3.1.1 Structure Characterization

Applying H$_2$-chemisorption to Ni–ZrO$_2$ after oxidation at 773 K and reduction at 673 K indicated an accessible metallic Ni surface area of 31.4 m^2 g^{-1} [68]. This results in a calculated Ni particle size of 21.5 nm (implying spherical Ni particles) which is in reasonable agreement with the particle size found by TEM, as described below. Note however, that for XRD and TEM analysis, the reduced Ni–ZrO$_2$ had to be exposed to air prior to the measurements. Due to easy reoxidation, at least the outer shell of the Ni nanoparticles is thus not expected to remain in the metallic state.

The diffractogram in Fig. 1a) displays mostly reflections characteristic of monoclinic ZrO$_2$. Small peaks of cubic NiO (at 37.3° and 43.2°) are visible, whereas those of metallic Ni (at 44.4° and 51.8° and also expected to be weak) are overlapping with ZrO$_2$ reflections. According to TEM, the particles of the monoclinic ZrO$_2$ support have a diameter of about 50–100 nm (Fig. 1b). At low magnification the low Z-contrast between zirconia and Ni or NiO prevents the unambiguous identification of Ni/NiO particles and EDX was thus applied to locate them. Typically, the particles consisted of a Ni core and a disordered shell (with a thickness of up to several nanometers). The fcc Ni particle core is imaged with lattice resolution in Fig. 1b. According to XRD, the shell must be NiO. The Ni/NiO particles were evenly distributed on the zirconia support and their size ranged from about 10–30 nm, but most of them had a diameter of about 20 nm.

3.1.2 CO Adsorption

In the next step, the interaction of the technological catalyst with CO was studied by FTIR. For the adsorption experiments Ni–ZrO$_2$ was pre-reduced in 5 mbar H$_2$ at 673 K.
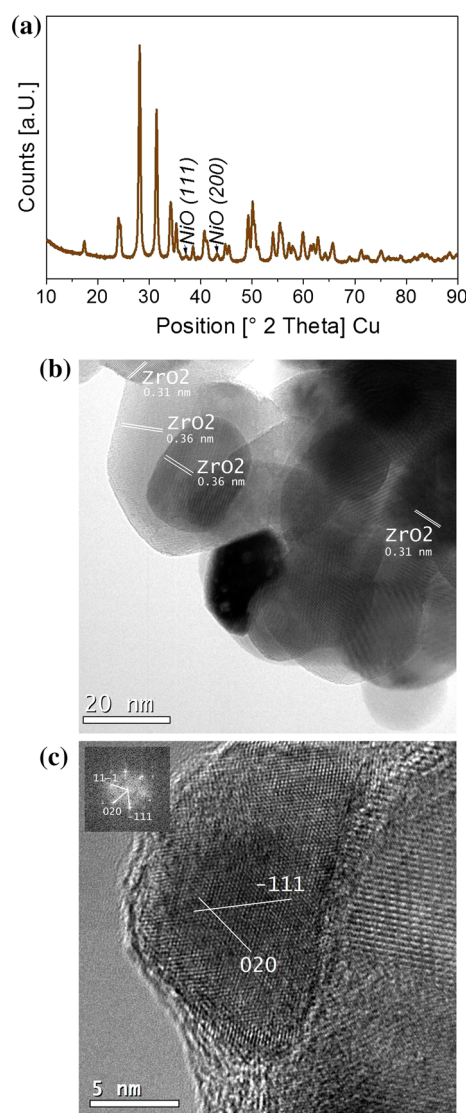

Fig. 1 XRD (**a**) und TEM (**b**, **c**) of technological Ni–ZrO$_2$ after ex situ oxidation at 773 K followed by reduction at 673 K. The sample was exposed to air prior to XRD and TEM, however. The XRD pattern shows reflections characteristic of monoclinic ZrO$_2$ and cubic NiO. TEM reveals ZrO$_2$ (**b**) and Ni/NiO particles (**c**) of about 50 and 20 nm diameter, respectively

Afterwards 0.1, 0.5, 1.0, and 5.0 mbar CO were dosed at 300 K and for each respective pressure FTIR spectra were acquired (Fig. 2a). Additionally, one spectrum was recorded after evacuation to less than 2×10^{-6} mbar.

The peaks at 2185–2190 and 2164 cm^{-1} are attributed to Zr^{4+}–CO and Ni^{2+}–CO, respectively. With increasing CO pressure, the Zr^{4+}–CO peak grows and obscures the Ni^{2+}–CO peak. The band at 2060 cm^{-1} appearing at 0.1 mbar pressure is attributed to linearly adsorbed CO on Ni^0 and the broad band(s) below 2000 cm^{-1} are attributed to threefold hollow bonded CO on Ni^0 [69–71]. The band at 2120 cm^{-1}, shifting to 2127 cm^{-1} with increasing CO pressure, is attributed to Ni$^+$–CO. The unusual oxidation
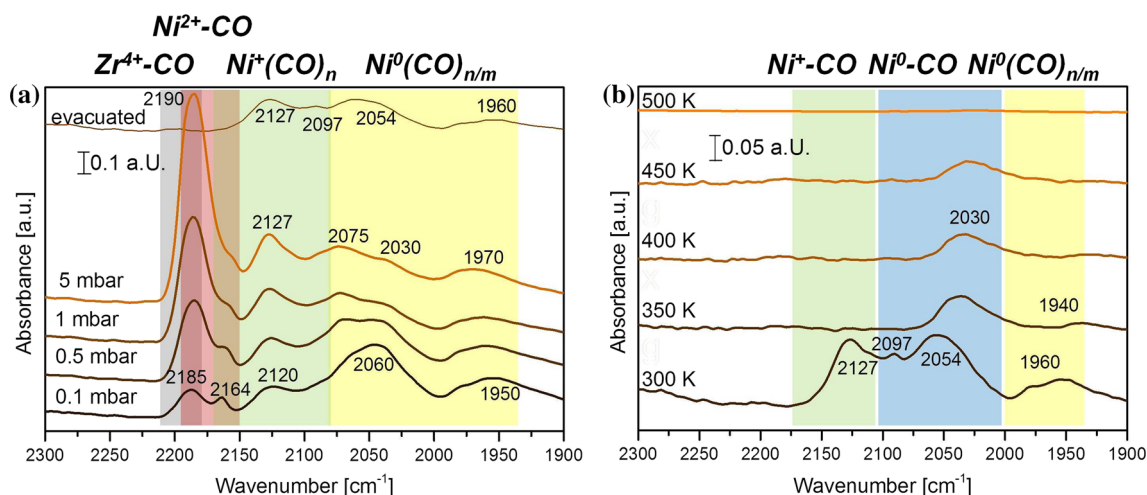
Fig. 2 a FTIR spectra of Ni–ZrO$_2$ (reduced in 5 mbar H$_2$ at 673 K) acquired at 300 K during CO adsorption at different pressures and after evacuation. **b** The thermal stability of adsorbed CO was followed by recording FTIR spectra upon annealing in vacuum (heating rate of 10 K min^{-1})

state of Ni$^+$ is stabilized by the ligand CO [72]. Indeed, the decreasing peaks of CO on Ni^0 and Ni^{2+} and the increasing CO–Ni$^+$ peak are due to a surface reaction in the presence of CO (Ni^{2+} + Ni^0 → 2 Ni$^+$; see Kasal et al. [72]).

After evacuation, Ni$^+$–CO as well as linear and hollow bonded CO on Ni^0 partly remain on the surface. Overall, CO FTIR indicates that, in agreement with XAS measurements [68], both reduced and oxidized Ni species are present on the catalyst surface and that NiO reduction in H$_2$ is not complete at 673 K.

This may explain why CO dissociation (and resulting carbon poisoning) is not occurring for the technological catalyst upon room temperature CO adsorption. When the CO dosing was repeated (after evacuation) basically the same IR spectra were obtained. As shown below, the supported (fully metallic) Ni nanoparticles prepared in UHV dissociated CO already around room temperature.

In a consecutive experiment (after evacuation) CO desorption was monitored via heating to elevated temperatures. In Fig. 2b the thermal stability of adsorbed CO was followed by recording FTIR spectra during heating with a rate of 10 K min^{-1} in high vacuum. CO desorbed from Ni$^+$ between 300 and 350 K, adsorbed multiply coordinated CO on Ni^0 vanished at 400–450 K (in agreement with single crystal data [64, 73]) and at 450–500 K all CO (including linear) had desorbed from Ni–ZrO$_2$.

3.1.3 Methane Dry Reforming (MDR)

The most straightforward and direct measurement of the thermal stability of the Ni–ZrO$_2$ catalyst is via its catalytic activity at high temperature, such as during methane dry reforming:

$$CH_4 + CO_2 \leftrightarrows 2CO + 2H_2 \quad \Delta H^{\circ}_{298K} = +261 kJ/mol.$$
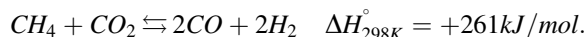
After oxidation at 773 K in O$_2$/Ar followed by reduction at 873 K in H$_2$/Ar the Ni–ZrO$_2$ catalyst was exposed to CH$_4$:CO$_2$:Ar = 10/10/80 with a total flow rate of 25 ml min^{-1} at 873 K for 24 h (total pressure 1 bar). Figure 3 highlights the analysis obtained by gas chromatographic (GC) flame ionization detection (FID) and thermal conductivity (TCD) detection of reactants and products during methane dry reforming. It was observed that the CH$_4$ and CO$_2$ conversion as well as the production rate of H$_2$ and CO hardly changed over time. The H$_2$:CO ratio achieved was below one due to reverse water gas shift (RWGS) as a side reaction ($CO_2 + H_2 \leftrightarrows CO + H_2O$; $\Delta H^{\circ}_{298K} = +41 kJ/mol$). The C-balance (indicating coke formation when being below one) increased to nearly one during the first 3 h.

The turn-over-frequency (TOF) for H$_2$ production based on the metallic Ni surface area after reduction at 873 K, normalized to the number of surface nickel atoms assuming 1.59×10^{19} nickel atoms/m^2 [74], was initially 1.2 s^{-1}, 1.2 s^{-1} after 3 h time on stream and 1.0 s^{-1} after 24 h time on stream.

Figure 4a shows a TEM image of Ni–ZrO$_2$ taken after dry reforming at 873 K (24 h). Filamentous carbon has formed and some Ni particles are located on top of the carbon nanofibers, tubes or rods.

After 24 h reaction in methane and carbon dioxide, temperature programmed oxidation (TPO) was performed with a heating rate of 5 K min^{-1} in 20 % O$_2$ in Ar. TPO provides information about the amount of coke formed during the reaction and the temperature which is required to burn off the carbon species. This temperature is
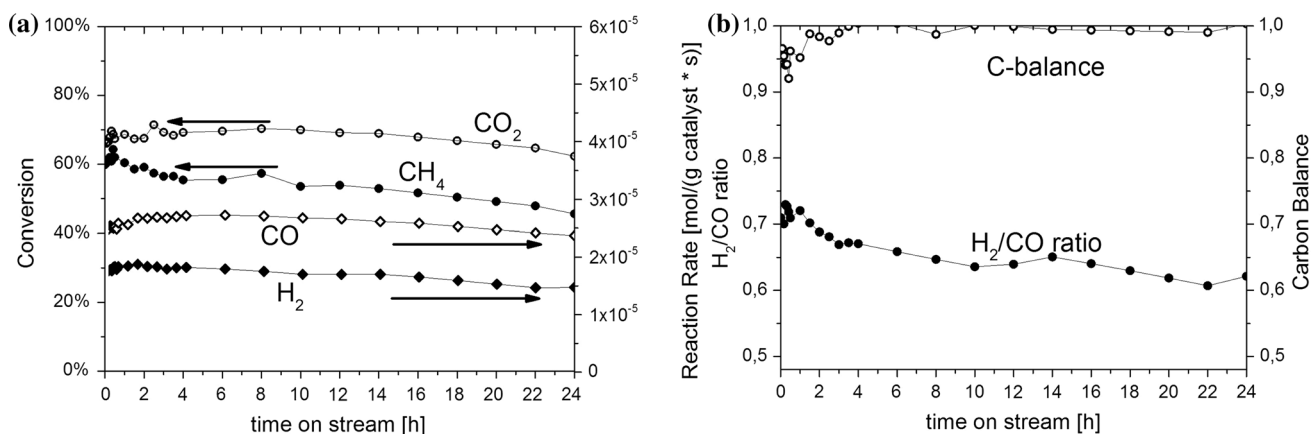
(a)

(b)

Fig. 3 **a** Conversion of reactants and reaction rate of hydrogen and carbon monoxide production and **b** H_2/CO ratio and carbon balance over Ni–ZrO_2 for methane dry reforming reaction at 873 K; feed composition: $CH_4:CO_2:Ar = 10/10/80$; feed flow rate = 25 ml min^{-1}

Fig. 4 **a** TEM image of coked Ni–ZrO_2 and **b** temperature programmed oxidation with 20 % O_2 in Ar after exposure to CH_4 and CO_2 at 873 K

(a)

(b)
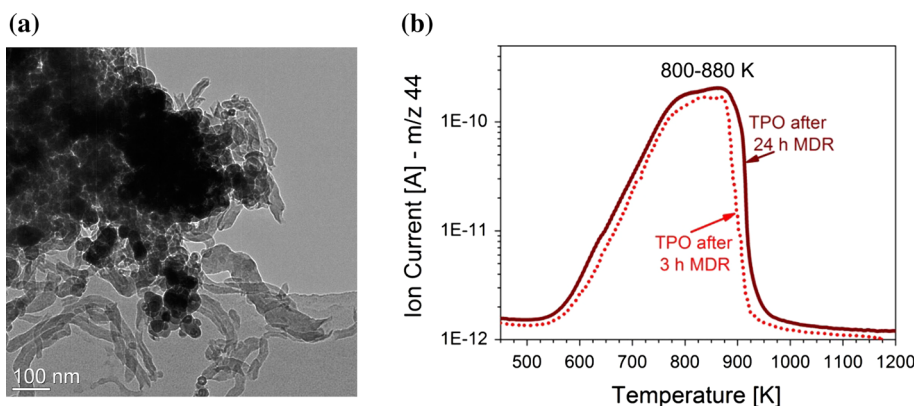
characteristic for the bond strength of carbon to the catalyst's surface and for the nature of the carbon species. Figure 4b shows the CO_2 production during TPO after dry reforming. Temperatures of about 800–880 K are needed to oxidize most of the coke. According to the literature, the first CO_2 evolution maximum around 800–810 K can be assigned to graphitic carbon [75]. The CO_2 evolution around 870–880 K can be assigned to the oxidation of whisker-type carbon which does not deactivate the nickel surface but rather causes a breakdown of the catalyst by pore plugging [76]. It is also interesting to note that the TPO acquired after a reaction time of 3 h is nearly identical indicating that coke deposition occurs rather rapid. Apparently, this type of coking does not deactivate the Ni surface but rather grows whiskers. The major problem of this catalyst is thus not the drop in catalytic activity but rather the physical blocking of the tube reactor. This was indeed observed when increasing the amount of catalyst in other catalytic tests.

The activation of CH_4 and CO_2 as well as the reaction of these molecules on transition metal surfaces have been studied in great detail [34–39]. Methane activation on transition metal surfaces is characterized by a high

activation barrier, a low sticking coefficient and a high hydrogen kinetic isotope effect [77]. Wang et al. [35] investigated the reaction pathways for MDR on Ni(111) by density functional theory and suggested a simplified reaction mechanism. The rate determining step was found to be CH_4 dissociative adsorption. CH_3, which is produced by CH_4 dissociation prefers to dehydrogenate into CH_2 which prefers to dehydrogenate to CH. However, CH prefers to be oxygenated to CHO by surface oxygen, which is formed by CO_2 dissociation (without surface oxygen, dehydrogenation to C and H occurs). Dehydrogenation of CHO into H and CO then has a very low energy barrier on Ni(111). The mechanism proposed in this analysis of unsupported Ni is depicted in Fig. 5.
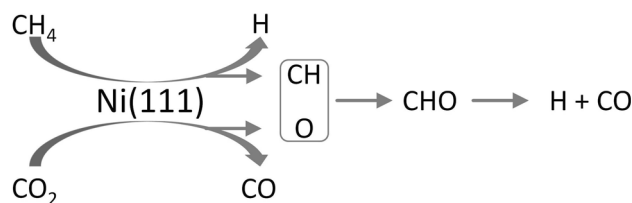

Fig. 5 Simplified mechanism of CO_2 reforming on Ni(111). Adapted from Wang et al. [35]

On supported catalysts, it is expected that the step of methane decomposition occurs on the metal particles [38, 39] while CO_2 activation likely occurs on the support [36, 37, 78, 79]. Thus, the reaction between CH_x and "activated" CO_2 might take place on the metal-support interface. For MDR over $Pt/ZrO_2/Al_2O_3$ catalysts, a kinetic model based on this dual mechanism was successfully correlated with experimental data [7].

For CO_2 activation, support materials with basic OH species increase the interaction of CO_2 with the support and, therefore, increase the CO_2 concentration on the surface, e.g. in form of carbonates, and also increase CO_2 affinity for surface carbon which minimizes carbon accumulation $(CO_2 + C \leftrightarrows 2CO \quad \Delta H_{298K}^{\circ} = +171 kJ/mol)$. [80].

Altogether, the reaction network is quite complex, and reforming, RWGS and Boudouard may occur simultaneously. Their relative contribution will strongly depend on the exact reaction conditions which also affect the state of the metal (CH_x coverage), of the support oxide (adsorbed carbonates, formates and OH), and of the metal-oxide interface.

3.1.4 Operando Spectroscopy During Methane Steam Reforming (MSR)

The high reaction temperature of MDR (873 K) prevented to acquire operando FTIR spectra. In the following operando results are presented for methane steam reforming (MSR) on $Ni–ZrO_2$,

$$CH_4 + H_2O \rightarrow CO + 3H_2 \quad \Delta H_{298K}^{\circ} = +206 kJ/mol,$$
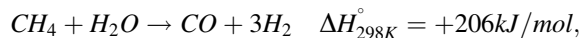
obtained by simultaneous FTIR and MS measurements (Fig. 6). The pre-reduced catalyst was heated in a mixture of CH_4 and H_2O (~ 1.2 bar with a ratio of 1/3) from 300 to 673 K. As reference state, the FTIR spectrum of the reduced catalyst prior to the reaction is included.

The MSR reaction products are again CO and H_2, i.e. both methane and water must be activated, e.g. via CH_4 dehydrogenation (dissociative adsorption) and H_2O dissociation. Once more, water gas shift (WGS; $CO + H_2O \leftrightarrows CO_2 + H_2 \quad \Delta H_{298K}^{\circ} = -41 kJ/mol$) may occur, accounting for the CO_2 byproduct [38, 39].

On the reduced catalyst a small amount of bridged bidentate carbonates (at 1630, 1430 and 1230 cm^{-1}) as well as bridged OH-groups (below 3700 cm^{-1}) were observed by FTIR at room temperature (all typical of "residual" adsorbates on the ZrO_2 support). In the reaction mixture at 373 K adsorbed water (broad peak around 1630 cm^{-1}) but also adsorbed CH_3 and CH_2 groups were detected (i.e. methane decomposition starts already at low temperature), in addition to OH-groups. By further

increasing the temperature to 573 K adsorbed water vanished from the surface, while the CH_x species remained. At about 623 K, H_2, CO and CO_2 formation (i.e. MSR and WGS) set in (detected by MS) and a new type of bidentate bicarbonate appeared on the surface (~ 1530 cm^{-1}). The formed CO_2 thus accounts for the (re)appearance of the (bi)carbonates. When temperature and reactivity were increasing the vibrations of bidentate *bi*carbonates shifted from 1550 to 1520 and from 1330 to 1350 cm^{-1}. During 2 h of reaction at 673 K neither the adsorbates nor the reactivity towards MSR were changing, i.e. no deactivation was observed.

In summary, FTIR detected activated CH_4 (CH_3 and CH_2), activated water (OH), as well as different bidentate (bi)carbonate species. The latter certainly originate from the water gas shift side reaction. Indeed, we have previously examined the reaction of the product CO with surface OH groups on an oxide surface, forming surface (bi)carbonates [79]. However, it remains unclear whether the bidentate (bi)carbonates are intermediates in the formation of CO [36, 37] or rather spectator species originating from readsorption of CO_2. Additional concentration modulation experiments [81] would be required for a conclusive answer.

3.2 UHV-Grown Model Catalysts of $Ni–ZrO_2/Pd_3Zr(0001)$

3.2.1 Preparation and Characterization

As described in the experimental section, the ZrO_2 model support was prepared by oxidation/annealing of an adequate intermetallic compound, either $Pd_3Zr(0001)$ or $Pt_3Zr(0001)$, producing an ultrathin ZrO_2 (O–Zr–O) trilayer. Using an electron beam evaporator, Ni nanoparticles were then grown on top of the ultrathin ZrO_2 layer. The amount of deposited Ni (nominal thickness 3 Å) was controlled by a calibrated quartz microbalance. For further details concerning ZrO_2 film preparation and cluster growth we refer to references [65, 66, 82, 83].

The growth of the current ZrO_2 thin film was monitored by XPS. Figure 7 shows Zr 3d spectra of the clean Pd_3Zr alloy (left), of the ultrathin (O–Zr–O trilayer) ZrO_2 (middle; after oxidation in 1×10^{-7} mbar of O_2 at 673 K for 30 min, followed by annealing in UHV at 1073 K for 20 min), and after deposition of 3 Å Ni at 300 K onto the ZrO_2 film (right).

The Pd_3Zr alloy (left) is characterized by a peak at a BE of 179.8 eV, after oxidation there are additional components at 181.2 eV and 182.5/183.1 eV, due to the trilayer ZrO_2 film and thicker ZrO_2 clusters, respectively. Although oxide clusters are the minority species (about 10 % surface coverage), due to their thickness of several nanometers
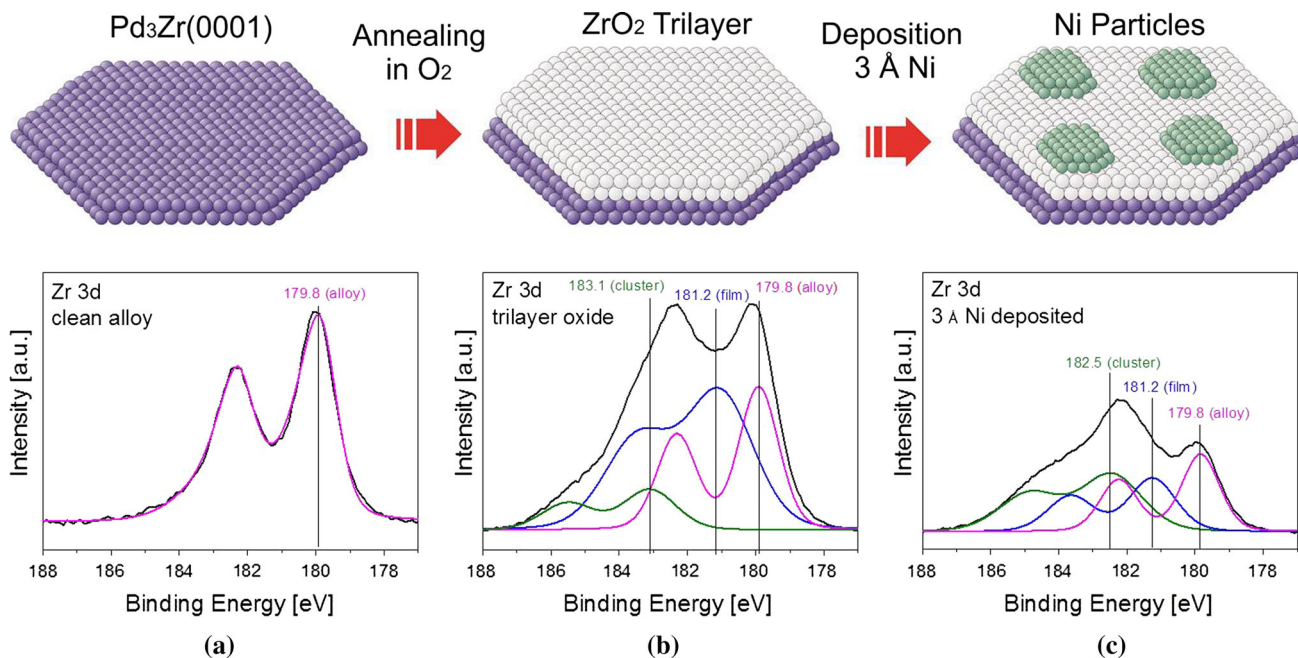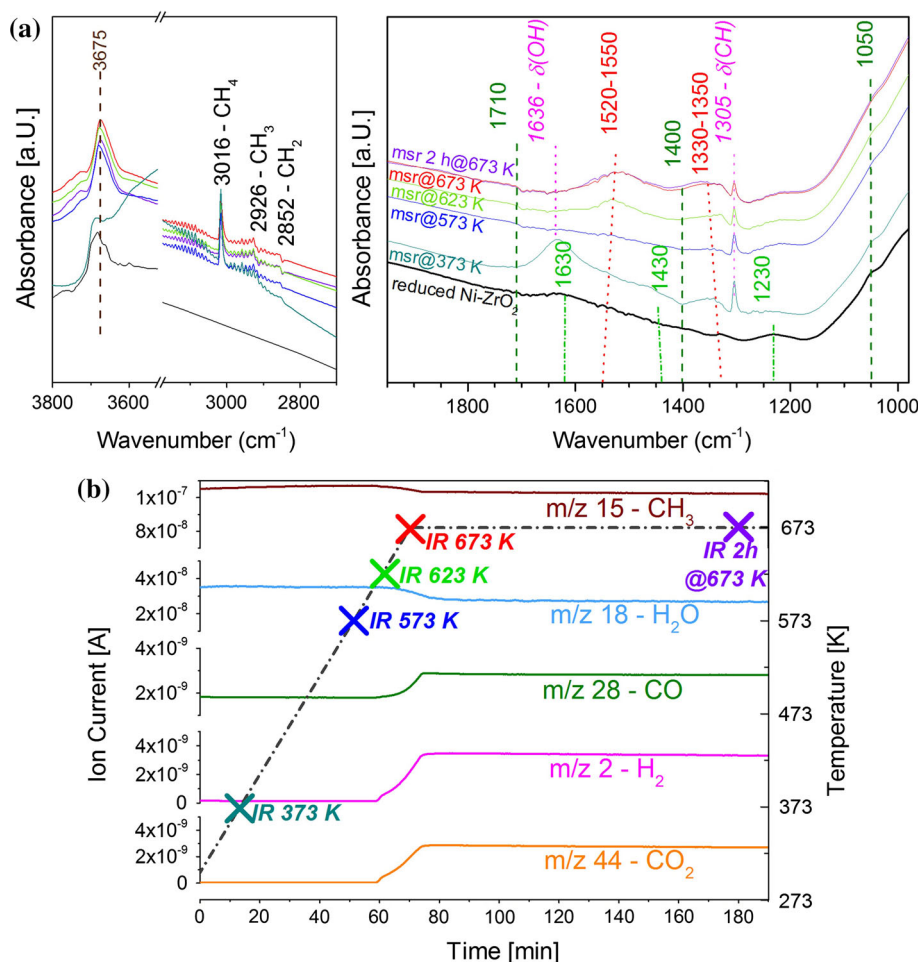
Fig. 7 Preparation of the Ni–ZrO₂/Pd₃Zr(0001) model catalyst followed by XPS. *Top*: schematic illustration. *Bottom*: (**a**) XPS Zr3d signal of the clean alloy, and of the oxide before (**b**) and after Ni deposition (**c**). All spectra were fitted to distinguish between the respective components

their contribution to the spectra is comparably larger (photoelectrons originate from multiple ZrO_2 layers instead of a single ZrO_2 layer). Using a laboratory X-ray source the inelastic mean free path (IMFP) of the photoelectrons is about 2 nm (sampling depth ~6 nm), thus the spectrum is still dominated by the alloy substrate. For more surface sensitive (synchrotron-based) XP spectra we refer to our study of the related ultrathin zirconia film on Pt_3Zr [65]. The major difference of the two films is the higher surface defect density of ZrO_2/Pd_3Zr and, while for Pd_3Zr the interlayer between the alloy and oxide is roughly stoichiometric, for Pt_3Zr there is an interlayer of pure Pt.

Figure 8a,b shows the LEED pattern (corresponding to Fig. 7a,b) measured with an electron energy of 79 eV, revealing the well-ordered (epitaxial) structure of the ultrathin oxide on the (0001) Pd_3Zr surface. It displays the hexagonal reciprocal lattice of the oxide film (red hexagon) and of the alloy substrate (blue hexagon), with a ratio of the reciprocal lattices of oxide to substrate a_{ox}/a_{met} of 1.556. According to scanning tunneling microscopy (STM) this corresponds to real space lattice parameters of 0.56 and 0.351 nm for oxide and alloy, respectively [66]. Furthermore, there are two oxide hexagonal lattices, rotated by an angle of 6.7° which correlates perfectly with the Fourier transform of STM images of the oxide film, indicating two rotational domains [65]. A structure model of the ZrO_2 film on Pd_3Zr, derived from combined STM and by density functional theory (DFT) studies [66], is shown in Fig. 8c. Based on the structural information, the specific XPS binding energies of (alloy supported) ZrO_2 trilayers and of thicker ZrO_2 layers could be explained by density functional calculations [65]. These XPS binding energies provide a useful reference for alloy (metal) supported ultrathin ZrO_2 as well as for more bulk-like ZrO_2 clusters.

Deposition of 3 Å Ni at room temperature induces a significant change in the Zr 3d region (Fig. 7c, top). Based on corresponding STM studies [83] of Ni cluster growth on ZrO_2/Pt_3Zr we expect that most (>80 %) of the ZrO_2 support is covered by Ni, either in the form of closely spaced nanoparticles or, in case of coalescence, by large (~10 nm) connected Ni islands (with a height of about 0.2 nm). Locally, the oxide support is still accessible by the gas phase, however. On ZrO_2/Pd_3Zr, the nucleation density (~4×10^{13} cm^{-2}) is about twice as high, so that a (nearly) closed and thin (~0.1 nm) Ni film is obtained.

The fitted Zr 3d region of the Ni-covered ZrO_2/Pd_3Zr is shown in Fig. 7c. It is evident that the (relative) intensity of the ZrO_2 trilayer film (and that of the alloy substrate) strongly decreased while the signal of the ZrO_2 clusters was much less affected (note that the exact geometry between sample, X-ray source and analyzer may vary between measurements, so that relative rather than absolute intensities should be compared).

The pronounced differences in the oxide trilayer and oxide cluster signals after Ni deposition can be explained by the different interplay between Ni and the underlying ZrO_2. When Ni grows on the ultrathin oxide it attenuates the photoelectrons escaping from the underlying trilayer of ZrO_2 (and from the Pd_3Zr alloy beneath), as well as modifying the electronic and geometric structure of the trilayer (presumably because of its strong binding both to Zr and O [83]). The ZrO_2 clusters exhibit a more bulk-like electronic structure, and seem less influenced by deposited Ni. This may be due, apart from their size of ~10 nm, to a different growth mode of Ni on ZrO_2 clusters (e.g. with a lower nucleation density leaving more open space between Ni particles). A clear answer cannot be given at this point.

Photoemission spectra of the Ni 2p region (cf. Fig. 10) show that nickel is deposited in its metallic form, i.e. with the 2p region showing the satellite structure at 858.2 eV characteristic of metallic nickel. Note that on the technological catalyst, even after reduction at 673 K, part of the Ni surface remained oxidic.
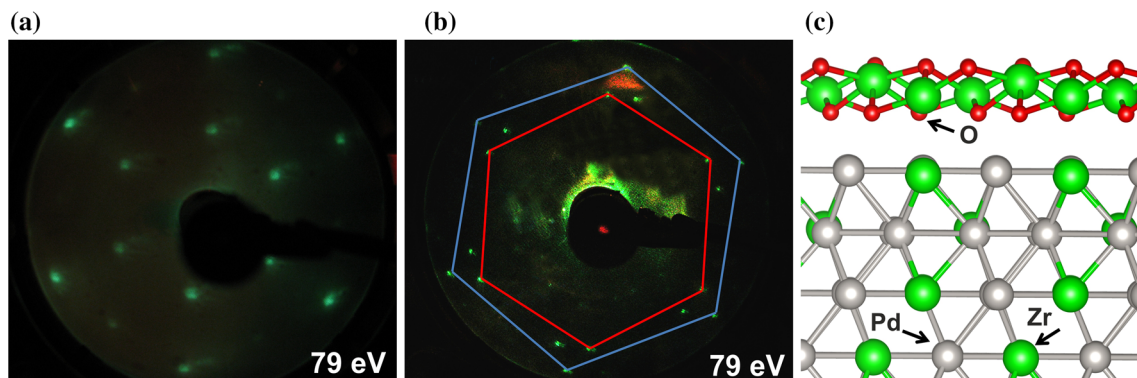

Fig. 8 (**a**, **b**) LEED pattern and (**c**) schematics of the ultrathin ZrO_2 (111) film on Pd_3Zr (0001) annealed at 1073 K [LEED: oxide lattice (*red*); alloy substrate (*blue*)]

3.2.2 CO Adsorption and Dissociation

CO is, of course, a product of reforming and it is also involved in the (reverse) water gas shift reaction. In order to examine the interaction of the model reforming catalyst with gaseous CO, the freshly prepared 3 Å Ni/ZrO$_2$/Pd$_3$Zr sample was transferred to the high pressure cell [49] and cooled with liquid nitrogen to 200 K. Then, CO PM-IRAS spectra were acquired under isothermal conditions from 10^{-6} mbar to 100 mbar. As described in more detail in Ref. [50], PM-IRAS only displays the surface adsorbed species, whereas the gas phase signal is removed. The measured spectra (Fig. 9a) show a gradual increase of the absorption signal (or coverage of) CO at 2075 cm^{-1}, which can be attributed to CO chemisorbed on top of individual nickel atoms. Signals of multiply-bonded CO ($\sim$1920 cm^{-1}) were very broad and weak. CO adsorption on the ZrO$_2$ trilayer (around 2190 cm^{-1} on powder ZrO$_2$; cf. Fig. 2) was not observed, due to its desorption temperature of 155 K [65].

After evacuation of the reaction chamber and measuring another PM-IRAS spectrum at 200 K, on-top CO was still detected [Fig. 9b; which is expected since CO desorbs from Ni(111) and Ni(100) at $\sim$425 K [64, 84]]. However, when the sample was gradually heated to higher temperatures in UHV, the signal of on-top CO vanished after heating to 300 K. Clearly, this cannot be due to CO desorption. Upon recooling and redosing 10^{-4} mbar (or higher) CO at 200 K the signal at 2075 cm^{-1} did not reappear, as shown in Fig. 9b. Possible explanations are either (1) that the Ni particles/islands had strongly sintered (less likely in view of the moderate temperatures) or (2) (more likely) that CO dissociated on

nickel and that the formed coke covered the metal surface and hindered CO (re-)adsorption.

In order to examine the exact reason of the disappearance of the PM-IRAS absorption signal upon annealing/redosing, a fresh Ni/ZrO$_2$/Pd$_3$Zr model catalyst was prepared and the surface was saturated with CO at 90 K already in the preparation chamber (50 L CO exposure). Afterwards XP spectra of the C1 s and Ni2p regions were measured which revealed a peak at 284.9 eV characteristic of molecular CO (Fig. 9c), as well as a peak at 852.7 eV characteristic of metallic Ni (not shown). Afterwards, the model catalyst was successively heated in UHV up to 550 K. As shown in Fig. 9c a shift in C1 s binding energy towards lower binding energies could be observed, from 284.9 eV at 90 K (molecular CO) to 283.9 eV at 550 K (characteristic of sp^2-bound carbon). This clearly shows that CO dissociates on nickel upon annealing, a well-known property, thereby forming a carbon over-layer on the nickel surface, which prevents further CO from adsorbing. During this experiment the Ni2p signal remained unaffected, i.e. there was no Ni sintering (which would reduce the intensity) and no formation of Ni carbide (which would induce a shift to 283.5 eV in C1 s [85]).

Previous studies of mbar pressure CO adsorption on supported Pd nanoparticles [52] and smooth and defect-rich Pd(111) single crystals [86, 87] have indicated the absence of CO dissociation on Pd. To confirm the hypothesis of coking on Ni, corresponding XPS experiments were thus performed for ZrO$_2$ supported Pd nanoparticles. As expected, upon heating the Pd nanoparticles up to 550 K, CO desorption ($\sim$420 K) but no CO dissociation (carbon deposits) were detected by IRAS and XPS.
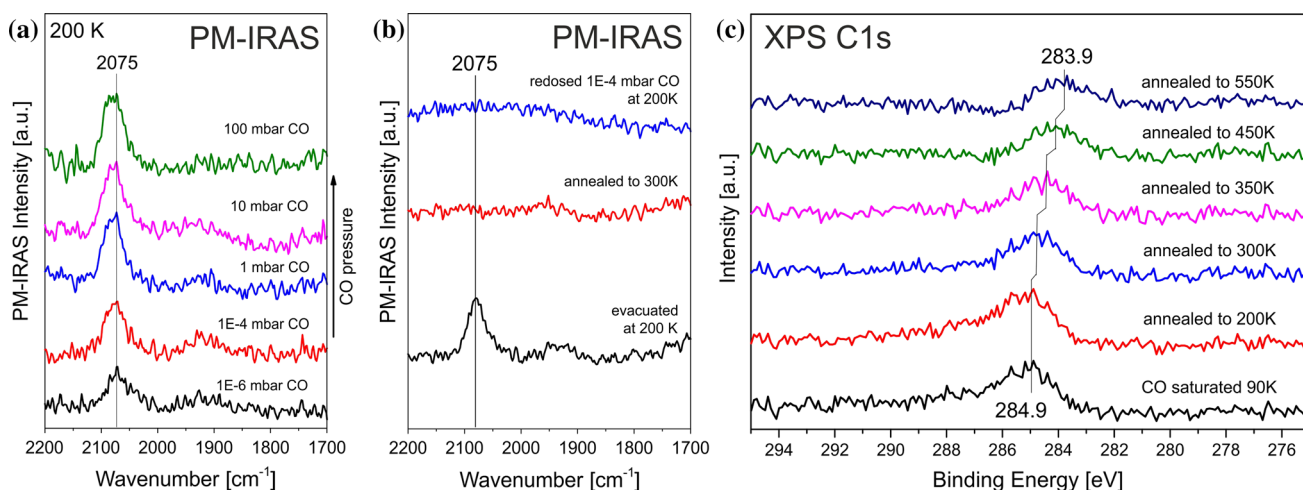

Fig. 9 CO adsorption on the Ni–ZrO$_2$/Pd$_3$Zr(0001) model catalyst monitored by PM-IRAS and XPS. **a** CO adsorption at 200 K at increasing pressure; **b** PM-IRAS signal after adsorption and evacuation, followed by heating to 300 K. Upon readsorption at 200 K the CO band at 2075 cm^{-1} did not reappear; **c** C1 s spectra of stepwise annealing of the CO saturated surface followed by XPS

3.2.3 Ni Nanoparticle Stability

The thermal stability of Ni particles on ZrO_2 was investigated using XPS (in this case for the Pt_3Zr substrate, however). Figure 10 shows the corresponding Ni2p spectra, acquired after Ni deposition and after annealing in UHV to 550 K. Apparently, the Ni nanoparticles were stable up to 550 K, as indicated by the nearly identical spectra. However, annealing to 800 K induced a $\sim$40 % decrease of the Ni 2p intensity, i.e. there was a strong "loss" of Ni. An apparent explanation would be a strong sintering of Ni nanoparticles. When the dispersion is reduced, the Ni2p signal decreases. However, it has been previously reported for ultrathin oxides that metal atoms may also diffuse through the ultrathin oxide and merge with the substrate, for example for Pd on alumina/NiAl [88], for Pd atoms on SiOx [89] and for Pd on thin FeO(111) film [90].

Indeed, corresponding STM studies of Ni clusters on ZrO_2/Pt_3Zr indicated that above 500 K metal atoms migrated through the oxide support into the alloy substrate [83]. We have thus modeled the XPS intensities of a 3 Å Ni layer above and below the ZrO_2 support oxide. The calculations indicate that Ni migration to below the trilayer would indeed result in a $\sim$40 % intensity decrease.

Once more, to confirm the hypothesis of "sub-oxide migration", corresponding XPS experiments were performed for ZrO_2 supported Pd nanoparticles (not shown). Upon heating the Pd nanoparticles to 500 K, the Pd 3d signal remained unaffected whereas annealing to 800 K again led to a $\sim$32 % decrease of the XPS Pd 3d signal. Consequently, at high temperature the Pd atoms also migrated through the ultrathin oxide into the underlying alloy. Further experiments using low energy ion scattering (LEIS) or synchrotron XPS (which are both more surface sensitive than our laboratory XPS) are required to examine the "sub-oxide migration" in more detail.

4 Discussion

We have examined Ni–ZrO_2 reforming catalysts using both technological (powder) catalysts as well as model (single crystal based) catalysts [50, 57]. Both approaches have their specific benefits, the first providing results that may be technologically relevant and the latter providing access to examining specific processes on an atomic/molecular level. In both cases, similar characterization methods have been employed, e.g. microscopy/diffraction for structure analysis (HRTEM, XRD, LEED), X-ray photoelectron spectroscopy or fluorescence for composition analysis (XPS, EDX), and infrared spectroscopy and temperature-programmed methods for adsorbate characterization (FTIR, PM-IRAS, TPO).

The surface science approach to heterogeneous catalysis often provides very detailed insight into elementary processes. Typically, the catalytic systems are somewhat simplified, such as well-ordered (ultra)thin planar oxide films with deposited clean and well-shaped metal nanoparticles [even though these are complex systems when compared to (noble) metal single crystals]. Such model systems are not only accessible by many surface sensitive methods but can also be modelled straightforward by theoretical methods, which are typically indispensable to interpret and thoroughly explain the experimental data [60, 65, 91, 92]. Whether this approach is a realistic scenario for technological catalysis remains a matter of debate because often rather the disordered structures exhibit the highest activity.

Apart from the materials or complexity gap, in many cases model studies are performed in UHV and at low temperature, leading to the "pressure gap". However, there are a number of "(near) atmospheric pressure surface science methods" available that enable to study functioning catalysts or, at least, model catalysts at elevated gas pressure and elevated temperature. Among the most frequently applied are PM-IRAS and SFG (sum frequency generation), both working up to 1 bar, and NAP-XPS (up to a few mbar) [50]. Nevertheless, operando spectroscopy is demanding in general, even for technological catalysts, and it is even more so for the low surface area model systems.

In the current case of Ni–ZrO_2 reforming catalysts, the Ni particles in the powder catalyst are rather large ($\sim$20 nm) and also the Ni islands on the model ZrO_2 cover most of the surface. Clearly, the "real" ZrO_2 is hydroxylated whereas the model oxide is not. Nevertheless, routines have been developed to create OH groups on UHV grown (ultra)thin oxides as well.
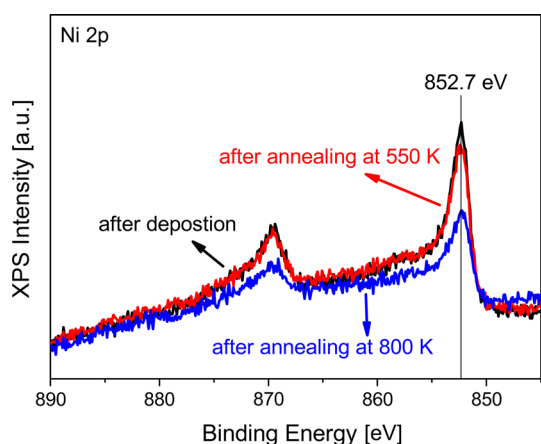

Fig. 10 Ni 2p XP spectra of the pristine Ni–ZrO_2/Pt_3Zr(0001) model surface, and after annealing to 550 and 800 K in UHV

With respect to CO adsorption at mbar pressure, differences were observed. CO adsorption on the technological Ni–ZrO$_2$ was reversible, i.e. CO could be adsorbed, desorbed at higher temperature, and readsorbed without significant loss of adsorption capacity. There were also no indications of CO dissociation. In contrast, the Ni nanoparticles grown in UHV dissociated adsorbed CO already around room temperature, which led to coking and irreversible CO adsorption, thus readsorbing CO on the poisoned surface was not possible. Taking into account the well-known fact that CO dissociation preferentially occurs on Ni edges/steps this difference may be explained by the partial oxidation of the technological Ni nanoparticles (even after reduction Ni-oxide species were detected in addition to metallic Ni). Thus, it is likely that the edges of technological Ni particles are oxidized which prevents CO dissociation. Unfortunately, CO-FTIR was not able to differentiate step and terrace sites and also HRTEM was unable to demonstrate this (due to sample air exposure prior to microscopy).

Under methane dry reforming conditions, when hydrogen is present at high temperature, the Ni particles (and their edges) are fully reduced and may also partly dissociate the reforming product CO. Clearly, CH$_4$ is the major carbon source and graphitic and whisker-type carbon were observed. Reverse water gas shift occurred in parallel and decreased the H$_2$/CO ratio. For methane steam reforming operando (FTIR and MS) studies were performed, indicating activated CH$_4$ (CH$_3$ and CH$_2$), activated water (OH), as well as different bidentate (bi)carbonate species. The latter originate from CO$_2$ resulting from the water gas shift side reaction but it is unclear whether these are intermediates or spectator species.

Ni–ZrO$_2$ model catalysts, prepared by surface science routes, turned out to be significantly more active for CO dissociation than their technological counterparts. When CO was adsorbed at pressures up to 100 mbar, both PM-IRAS and XPS revealed CO dissociation around room temperature and blocking of the Ni surface by carbon. This is most likely due to the fully metallic Ni particles whereas the technological particles were partially oxidized even after reduction at 673 K. CO adsorbed on the powder ZrO$_2$ at room temperature, but it did not on the trilayer ZrO$_2$ (CO desorption temperature of 155 K [65]).

A major limitation of most model systems is their thermal stability, however. For Ni–ZrO$_2$/Pd$_3$Zr the upper limit of stability is about 550 K. Around this temperature Ni atom migration through the ultrathin oxide (in)to the alloy substrate takes place and Ni is lost from the model catalyst surface. Such an effect does not occur for the technological catalyst and care must therefore be taken for model studies at higher temperature. Clearly, methane reforming cannot be studied in situ using the current model system.

5 Conclusions

We have examined Ni–ZrO$_2$ reforming catalysts, employing both technological materials (powders) as well as single crystal based surface science model catalysts. In both cases the Ni nanoparticles were rather large (20 nm or larger) but exhibited different properties with respect to CO dissociation. Whereas the partially oxidized "technological" Ni nanoparticles did not dissociate CO around room temperature, the fully metallic "surface science" Ni particles did, with the carbon deposits blocking further CO adsorption. For the technological samples methane dry and steam reforming were performed, with both reactions affected by (reverse) water gas shift, modifying the H$_2$/CO ratio and producing CO$_2$, respectively. For dry reforming whisker-type carbon was produced, operando studies of steam reforming revealed CH$_x$, OH, and different bidentate (bi)carbonate species. The limited thermal stability of model Ni–ZrO$_2$ prevented in situ reforming studies. Nevertheless, the XPS binding energies of alloy supported ultrathin trilayer (O–Zr–O) ZrO$_2$ as well as those of more bulk-like ZrO$_2$ clusters have been determined which provide useful reference data.

Altogether the combined technological and surface science approach is rewarding and it is fascinating to observe marked differences despite nominally the same Ni–ZrO$_2$ composition. Of course, "Ni–ZrO$_2$" is a very crude description missing important features like metal nanoparticle size and morphology, type of surface facets/steps, oxidation state, supporting oxide (surface) structure, hydroxylation, defect density, nature of metal-oxide interface sites, etc. Answering all these questions would provide the molecular details of how catalytic processes work and is thus a continuing mission.

References

1. Roh H-S, Eum I-H, Jeong D-W (2012) Low temperature steam reforming of methane over Ni–Ce(1 − x)Zr(x)O$_2$ catalysts under severe conditions. Renew Energy 42:212–216

2. Matsumura Y, Nakamori T (2004) Steam reforming of methane over nickel catalysts at low reaction temperature. Appl Catal A 258:107–114

3. Roh H-S, Platon A, Wang Y et al (2006) Catalyst deactivation and regeneration in low temperature ethanol steam reforming with Rh/CeO$_2$–ZrO$_2$ catalysts. Catal Lett 110:1–6

4. Kambolis A, Matralis H, Trovarelli A et al (2010) Ni/CeO$_2$–ZrO$_2$ catalysts for the dry reforming of methane. Appl Catal A 377:16–26

5. Montoya JA, Romero-Pascual E, Gimon C et al (2000) Methane reforming with CO$_2$ over Ni/ZrO$_2$–CeO$_2$ catalysts prepared by sol-gel. Catal Today 63:71–85

6. Pompeo F, Nichio NN, Souza MMVM et al (2007) Study of Ni and Pt catalysts supported on α-Al$_2$O$_3$ and ZrO$_2$ applied in methane reforming with CO$_2$. Appl Catal A 316:175–183

7. Souza MMVM, DaG Aranda, Schmal M (2001) Reforming of methane with carbon dioxide over Pt/ZrO$_2$/Al$_2$O$_3$ catalysts. J Catal 204:498–511

8. Bradford MCJ, Vannice MA, Ruckenstein E (1999) CO$_2$ reforming of CH$_4$. Catal Rev Sci Eng 41:1–42

9. Bitter JH, Seshan K, Lercher JA (1997) The state of zirconia supported platinum catalysts for CO$_2$/CH$_4$ reforming. J Catal 171:279–286

10. Berrocal GP, SaLM Da, Assaf JM et al (2010) Novel supports for nickel-based catalysts for the partial oxidation of methane. Catal Today 149:240–247

11. Otsuka K, Wang Y, Sunada E et al (1998) Direct partial oxidation of methane to synthesis gas by cerium oxide. J Catal 175:152–160

12. Gavrielatos I, Drakopoulos V, Neophytides SG (2008) Carbon tolerant Ni–Au SOFC electrodes operating under internal steam reforming conditions. J Catal 259:75–84

13. Molenbroek AM, Norskov JK, Clausen BS (2001) Structure and reactivity of Ni–Au nanoparticle catalysts. J Phys Chem B 105:5450–5458

14. Hyldtoft J, Norskov JK, Clausen BS (1999) Process for steam reforming of hydrocarbons. In: United States Patent. Haldor Topsoe A/S, Denmark

15. Ashok J, Subrahmanyam M, Venugopal A (2008) Hydrotalcite structure derived Ni–Cu–Al catalysts for the production of H$_2$ by CH$_4$ decomposition. Int J Hydrog Energy 33:2704–2713

16. Lazaro MJ, Echegoyen Y, Suelves I et al (2007) Decomposition of methane over Ni–SiO$_2$ and Ni–Cu–SiO$_2$ catalysts: effect of catalyst preparation method. Appl Catal A 329:22–29

17. Park EW, Moon H, Park M-S et al (2009) Fabrication and characterization of Cu–Ni-YSZ SOFC anodes for direct use of methane via Cu-electroplating. Int J Hydrog Energy 34:5537–5545

18. Suelves I, Lazaro MJ, Moliner R et al (2006) Characterization of NiAl and NiCuAl catalysts prepared by different methods for hydrogen production by thermo catalytic decomposition of methane. Catal Today 116:271–280

19. Chen J, Li X, Li Y et al (2003) Production of hydrogen and nanocarbon from direct decomposition of undiluted methane on high-nickeled Ni–Cu-alumina catalysts. Chem Lett 32:424–425

20. Echegoyen Y, Suelves I, Lazaro MJ et al (2007) Hydrogen production by thermocatalytic decomposition of methane over Ni–Al and Ni–Cu–Al catalysts: effect of calcination temperature. J Power Sour 169:150–157

21. Monzón A, Latorre N, Ubieto T et al (2006) Improvement of activity and stability of Ni–Mg–Al catalysts by Cu addition during hydrogen production by catalytic decomposition of methane. Catal Today 116:264–270

22. Cunha AF, Órfão JJM, Figueiredo JL (2009) Methane decomposition on Ni–Cu alloyed Raney-type catalysts. Int J Hydrog Energy 34:4763–4772

23. Li Z, Chen J, Zhang X et al (2002) Catalytic synthesized carbon nanostructures from methane using nanocrystalline Ni. Carbon 40:409–415

24. Kitla A, Safonova OV, Foettinger K (2013) Infrared studies on bimetallic copper/nickel catalysts supported on zirconia and ceria/zirconia. Catal Lett 143:517–530

25. Wolfbeisser A, Kloetzer B, Mayr L et al (2015) Surface modification processes during methane decomposition on Cu-promoted Ni–ZrO$_2$ catalysts. Catal Sci Technol 5:967–978

26. Chen J, Wu Q, Zhang J et al (2008) Effect of preparation methods on structure and performance of Ni/Ce0.75Zr0.25O2 catalysts for CH$_4$–CO$_2$ reforming. Fuel 87:2901–2907

27. Ebiad MA, Abd E-HDR, Elsalamony RA et al (2012) Ni supported high surface area CeO$_2$–ZrO$_2$ catalysts for hydrogen production from ethanol steam reforming. RSC Adv 2:8145–8156

28. Kumar P, Sun Y, Idem RO (2007) Nickel-based ceria, zirconia, and ceria–zirconia catalytic systems for low-temperature carbon dioxide reforming of methane. Energy Fuels 21:3113–3123

29. Kumar P, Sun Y, Idem RO (2008) Comparative study of Ni-based mixed oxide catalyst for carbon dioxide reforming of methane. Energy Fuels 22:3575–3582

30. Roh H-S, Potdar HS, Jun K-W (2004) Carbon dioxide reforming of methane over co-precipitated Ni–CeO$_2$, Ni–ZrO$_2$ and Ni–Ce–ZrO$_2$ catalysts. Catal Today 93–95:39–44

31. Sukonket T, Khan A, Saha B et al (2011) Influence of the catalyst preparation method, surfactant amount, and steam on CO$_2$ reforming of CH$_4$ over 5Ni/Ce0.6Zr0.4O$_2$ catalysts. Energy Fuels 25:864–877

32. Horvath A, Stefler G, Geszti O et al (2011) Methane dry reforming with CO$_2$ on CeZr–oxide supported Ni, NiRh and NiCo catalysts prepared by sol-gel technique: relationship between activity and coke formation. Catal Today 169:102–111

33. Ocampo F, Louis B, Kiennemann A et al (2011) CO$_2$ methanation over Ni–Ceria–Zirconia catalysts: effect of preparation and operating conditions. IOP Conf Ser Mater Sci Eng 19:012007/012001-012007/012011

34. Schulz LA, Kahle LCS, Delgado KH et al (2015) On the coke deposition in dry reforming of methane at elevated pressures. Appl Catal Gen 504:599–607

35. Wang S-G, Liao X-Y, Hu J et al (2007) Kinetic aspect of CO$_2$ reforming of CH$_4$ on Ni(1 1 1): a density functional theory calculation. Surf Sci 601:1271–1284

36. Bitter JH, Seshan K, Lercher JA (1997) The state of zirconia supported platinum catalysts for CO$_2$/CH$_4$ reforming. J Catal 171:279–286

37. Bitter JH, Seshan K, Lercher JA (1998) Mono and bifunctional pathways of CO$_2$/CH$_4$ reforming over Pt and Rh based catalysts. J Catal 176:93–101

38. Wei JM, Iglesia E (2004) Isotopic and kinetic assessment of the mechanism of reactions of CH4 with CO$_2$ or H$_2$O to form synthesis gas and carbon on nickel catalysts. J Catal 224:370–383

39. Wei JM, Iglesia E (2004) Mechanism and site requirements for activation and chemical conversion of methane on supported Pt clusters and turnover rate comparisons among noble metals. J Phys Chem B 108:4094–4103

40. Ertl G (1994) Reactions at well-defined surfaces. Surf Sci 299:742–754

41. Somorjai GA (1996) Modern surface science and surface technologies: an introduction. Chem Rev 96:1223–1235
42. King DA (1994) Chemisorption on metals—a personal review. Surf Sci 299:678–689
43. Goodman DW (1995) Model studies in catalysis using surface science probes. Chem Rev 95:523–536
44. Campbell CT (1997) Ultrathin metal films and particles on oxide surfaces: structural, electronic and chemisorptive properties. Surf Sci Rep 27:1–111
45. Henry CR (1998) Surface studies of supported model catalysts. Surf Sci Rep 31:235–325
46. Freund HJ, Baumer M, Kuhlenbeck H (2000) Catalysis and surface science: what do we learn from studies of oxide-supported cluster model systems? Adv Catal 45(45):333–384
47. Hayek K, Fuchs M, Klotzer B et al (2000) Studies of metal-support interactions with "real" and "inverted" model systems: reactions of CO and small hydrocarbons with hydrogen on noble metals in contact with oxides. Top Catal 13:55–66
48. Freund HJ, Bäumer M, Libuda J et al (2003) Preparation and characterization of model catalysts: from ultrahigh vacuum to in situ conditions at the atomic dimension. J Catal 216:223–235
49. Rupprechter G (2007) A surface science approach to ambient pressure catalytic reactions. Catal Today 126:3–17
50. Rupprechter G (2007) Sum frequency generation and polarization–modulation infrared reflection absorption spectroscopy of functioning model catalysts from ultrahigh vacuum to ambient pressure. Adv Catal 51(51):133–263
51. Baumer M, Libuda J, Neyman KM et al (2007) Adsorption and reaction of methanol on supported palladium catalysts: microscopic-level studies from ultrahigh vacuum to ambient pressure conditions. Phys Chem Chem Phys 9:3541–3558
52. Zorn K, Giorgio S, Halwax E et al (2011) CO oxidation on technological Pd–Al$_2$O$_3$ catalysts: oxidation State and activity. J Phys Chem C 115:1103–1111
53. Fottinger K, Van Bokhoven JA, Nachtegaal M et al (2011) Dynamic structure of a working methanol steam reforming catalyst. in situ quick-EXAFS on Pd/ZnO nanoparticles. J Phys Chem Letters 2:428–433
54. Haghofer A, Foettinger K, Girgsdies F et al (2012) In situ study of the formation and stability of supported Pd$_2$Ga methanol steam reforming catalysts. J Catal 286:13–21
55. Haghofer A, Foettinger K, Nachtegaal M et al (2012) Microstructural changes of supported intermetallic nanoparticles under reductive and oxidative conditions: an in situ X-ray absorption study of Pd/Ga$_2$O$_3$. J Phys Chem C 116:21816–21827
56. Haghofer A, Ferri D, Fottinger K et al (2012) Who is doing the job? unraveling the role of Ga$_2$O$_3$ in methanol steam reforming on Pd$_2$Ga/Ga$_2$O$_3$. Acs Catalysis 2:2305–2315
57. Fottinger K, Rupprechter G (2014) In situ spectroscopy of complex surface reactions on supported Pd–Zn, Pd–Ga, and Pd(Pt)–Cu nanoparticles. Acc Chem Res 47:3071–3079
58. Wolfbeisser A, Kloetzer B, Mayr L et al (2015) Surface modification processes during methane decomposition on Cu-promoted Ni–ZrO$_2$ catalysts. Catal Sci Technol 5:967–978
59. Rameshan C, Stadlmayr W, Weilach C et al (2010) Subsurface-controlled CO$_2$ selectivity of PdZn near-surface alloys in H-2 generation by methanol steam reforming. Angew Chem-Int Ed 49:3224–3227
60. Vogel D, Spiel C, Suchorski Y et al (2012) Local catalytic ignition during CO oxidation on low-index Pt and Pd surfaces: a combined PEEM, MS, and DFT study. Angew Chem-Int Ed 51:10041–10044
61. Opitz AK, Nenning A, Rameshan C et al (2015) Enhancing electrochemical water-splitting kinetics by polarization-driven formation of near-surface iron(0): an in situ XPS study on perovskite-type electrodes. Angew Chem-Int Ed 54:2628–2632
62. Guerrero-Perez MO, Banares MA (2002) Operando Raman study of alumina-supported Sb-V-O catalyst during propane ammoxidation to acrylonitrile with on-line activity measurement. Chem Comm 1292–1293
63. Weckhuysen BM (2003) Determining the active site in a catalytic process: operando spectroscopy is more than a buzzword. Phys Chem Chem Phys 5:4351–4360
64. Rupprechter G, Dellwig T, Unterhalt H et al (2001) CO adsorption on Ni(100) and Pt(111) studied by infrared-visible sum frequency generation spectroscopy: design and application of an SFG-compatible UHV-high-pressure reaction cell. Top Catal 15:19–26
65. Li H, Choi J-IJ, Mayr-Schmoelzer W et al (2015) Growth of an ultrathin zirconia film on Pt$_3$Zr examined by high-resolution X-ray photoelectron spectroscopy, temperature-programmed desorption, scanning tunneling microscopy, and density functional theory. J Phys Chem C 119:2462–2470
66. Choi JIJ, Mayr-Schmoelzer W, Mittendorfer F et al (2014) The growth of ultra-thin zirconia films on Pd3Zr(0001). J Phys Condens Matter 26:225003
67. Rupprechter G, Weilach C (2008) Spectroscopic studies of surface-gas interactions and catalyst restructuring at ambient pressure: mind the gap! J Phys Condens Matter 20:184019
68. Kitla A, Safonova OV, Foettinger K (2013) Infrared studies on bimetallic copper/nickel catalysts supported on zirconia and ceria/zirconia. Catal Lett 143:517–530
69. Sprunger PT, Besenbacher F, Stensgaard I (1995) STM investigation of the Ni(111) − c(4 × 2) − 2CO structure. Chem Phys Lett 243:439–444
70. Becker L, Aminpirooz S, Hillert B et al (1993) Threefold-coordinated hollow adsorption site for Ni(111)-\textit{c} (4\ifmmode\times\else\texttimes\fi{}2)-CO: a surface-extended x-ray-absorption fine-structure study. Phys Rev B 47:9710–9714
71. Davila ME, Asensio MC, Woodruff DP et al (1994) Structure determination of Ni(111)c(4 × 2)-CO and its implications for the interpretation of vibrational spectroscopic data. Surf Sci 311:337–348
72. Kasal PH, Bishop RJ Jr, Mcleod D Jr (1978) Ligand effects on the redox reactions in nickel- and copper-exchanged zeolites. J Phys Chem 82:279–285
73. Xu C, Koel BE (1995) Influence of alloyed Sn atoms on the chemisorption properties of Ni(111) as probed by RAIRS and TPD studies of CO adsorption. Surf Sci 327:38–46
74. Satterfield CN (1996) Heterogeneous catalysis in industrial practice. Krieger Pub, Florida
75. Bradford MCJ, Vannice MA (1996) Catalytic reforming of methane with carbon dioxide over nickel catalysts. I. Catalyst characterization and activity. Appl Catal A 142:73–96
76. Ginsburg JM, Piña J, El Solh T et al (2005) Coke formation over a nickel catalyst under methane dry reforming conditions: thermodynamic and kinetic models. Ind Eng Chem Res 44:4846–4854
77. German ED, Sheintuch M (2013) Predicting CH4 dissociation kinetics on metals: trends, sticking coefficients, H tunneling, and kinetic isotope effect. J Phys Chem C 117:22811–22826
78. Föttinger K, Schlögl R, Rupprechter G (2008) The mechanism of carbonate formation on Pd–Al$_2$O$_3$ catalysts. Chem Comm (Camb Engl) 320–322
79. Weilach C, Spiel C, Föttinger K et al (2011) Carbonate formation on Al$_2$O$_3$ thin film model catalyst supports. Surf Sci 605:1503–1509
80. Guerrero-Ruiz A, Sepulveda-Escribano A, Rodriguez-Ramos I (1994) Cooperative action of cobalt and MgO for the catalyzed reforming of CH$_4$ with CO$_2$. Catal Today 21:545–550
81. Haghofer A, Ferri D, Föttinger K et al (2012) Who is doing the job? Unraveling the role of Ga$_2$O$_3$ in methanol steam reforming on Pd$_2$Ga/Ga$_2$O$_3$. ACS Catal 2:2305–2315

82. Antlanger M, Mayr-Schmölzer W, Pavelec J et al (2012) Pt$_3$Zr(0001): a substrate for growing well-ordered ultrathin zirconia films by oxidation. Phys Rev B 86:035451

83. Choi JIJ, Wernfried M-S, Valenti I et al (2016) Metal Adatoms and Clusters on Ultrathin Zirconia Films. J Phys Chem C 120(18):9920–9932

84. Miller JB, Siddiqui HR, Gates SM et al (1987) extraction of kinetic-parameters in temperature programmed desorption—a comparison of methods. J Chem Phys 87:6725–6732

85. Wiltner A, Linsmeier C (2004) Formation of endothermic carbides on iron and nickel. Phys Status Solidi App Res 201:881–887

86. Kaichev VV, Morkel M, Unterhalt H et al (2004) C–O bond scission on "defect-rich and perfect" Pd(111)? Surf Sci 566:1024–1029

87. Dellwig T, Rupprechter G, Unterhalt H et al (2000) Bridging the pressure and materials gaps: high pressure sum frequency generation study on supported Pd nanoparticles. Phys Rev Lett 85:776–779

88. Napetschnig E, Schmid M, Varga P (2007) Pd, Co and Co–Pd clusters on the ordered alumina film on NiAl(110): contact angle, surface structure and composition. Surf Sci 601:3233–3245

89. Baron M, Stacchiola D, Ulrich S et al (2008) Adsorption of Au and Pd atoms on thin SiO$_2$ films: the role of atomic structure. J Phys Chem C 112:3405–3409

90. Meyer R, Lahav D, Schalow T et al (2005) CO adsorption and thermal stability of Pd deposited on a thin FeO(111) film. Surf Sci 586:174–182

91. Rupprechter G, Morkel M, Freund HJ et al (2004) Sum frequency generation and density functional studies of CO–H interaction and hydrogen bulk dissolution on Pd(111). Surf Sci 554:43–59

92. Weilach C, Kozlov SM, Holzapfel HH et al (2012) Geometric arrangement of components in bimetallic PdZn/Pd(111) surfaces modified by CO adsorption: a combined study by density functional calculations, polarization-modulated infrared reflection absorption spectroscopy, and temperature-programmed desorption. J Phys Chem C 116:18768–18778